ACS APPLIED MATERIALS & INTERFACES

www.acsami.org

Research Article

Graphene-Capped Liquid Thin Films for Electrochemical Operando X-ray Spectroscopy and Scanning Electron Microscopy

Lorenz J. Falling,* Rik V. Mom, Luis E. Sandoval Diaz, Siamak Nakhaie, Eugen Stotz, Danail Ivanov, Michael Hävecker, Thomas Lunkenbein, Axel Knop-Gericke, Robert Schlögl, and Juan-Jesús Velasco-Vélez*

Cite This: *ACS Appl. Mater. Interfaces* 2020, 12, 37680−37692

Read Online

ACCESS | Metrics & More | Article Recommendations | Supporting Information

ABSTRACT: Electrochemistry is a promising building block for the global transition to a sustainable energy market. Particularly the electroreduction of CO_2 and the electrolysis of water might be strategic elements for chemical energy conversion. The reactions of interest are inner-sphere reactions, which occur on the surface of the electrode, and the biased interface between the electrode surface and the electrolyte is of central importance to the reactivity of an electrode. However, a potential-dependent observation of this buried interface is challenging, which slows the development of catalyst materials. Here we describe a sample architecture using a graphene blanket that allows surface sensitive studies of biased electrochemical interfaces. At the examples of near ambient pressure X-ray photoelectron spectroscopy (NAP-XPS) and environmental scanning electron microscopy (ESEM), we show that the combination of a graphene blanket and a permeable membrane leads to the formation of a liquid thin film between them. This liquid thin film is stable against a water partial pressure below 1 mbar. These properties of the sample assembly extend the study of solid−liquid interfaces to highly surface sensitive techniques, such as electron spectroscopy/microscopy. In fact, photoelectrons with an effective attenuation length of only 10 Å can be detected, which is close to the absolute minimum possible in aqueous solutions. The in-situ cells and the sample preparation necessary to employ our method are comparatively simple. Transferring this approach to other surface sensitive measurement techniques should therefore be straightforward. We see our approach as a starting point for more studies on electrochemical interfaces and surface processes under applied potential. Such studies would be of high value for the rational design of electrocatalysts.

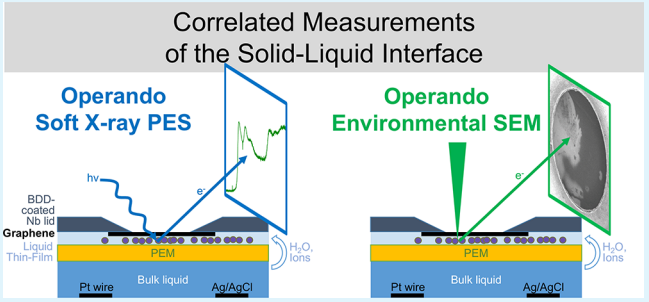

KEYWORDS: *solid−liquid interface, graphene, operando, X-ray spectroscopy, scanning electron microscopy, near ambient pressure, electrochemistry, proton exchange membrane*

INTRODUCTION

The solid−liquid interface plays an important role in technical processes like electroplating, etching, or electrocatalysis as well as biological and environmental processes such as corrosion, ice formation, or transport phenomena across lipid membranes. In all of them, the interaction between a solid surface and the covering layer of solvated species is crucial. Visualizing this interface with spectroscopy or imaging methods is very desirable but poses a fundamental challenge. Either the probe penetrates bulk layers of liquid and a small part of the signal is obtained from the interface, like it is the case for hard X-rays and infrared light, or the probe is surface sensitive and even thin layers of liquid prevent the probe or the measurand from reaching the interface, as is the case for soft X-rays or electron microscopy. Finding technical solutions is challenging.

Attempts to overcome these limitations took different avenues. The first is to enhance the signal from the interface, like in surface-enhanced Raman spectroscopy[1] or sum frequency generation.[2] This approach is elegant, but features of vibrational spectroscopy are not element specific and the nontrivial signal enhancement inside plasmonic cavities impedes quantification. The second approach is to reduce the thickness of the liquid layer and to use core-level spectroscopy. The dip-and-pull method in combination with tender X-rays[3] is a good example of that (for comparison see Table 1). The third approach is to reduce the thickness of the solid. Graphene-capped microchannels[4,5] or an electrochemical in-situ cell with graphene windows[6−8] used exactly that

Received: May 7, 2020
Accepted: July 23, 2020
Published: July 23, 2020

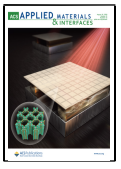

https://dx.doi.org/10.1021/acsami.0c08379
ACS Appl. Mater. Interfaces 2020, 12, 37680−37692

Table 1. Benefits and Drawbacks of Existing Approaches in Comparison

	Benefits	Drawbacks
Dip and pull	⊕⊕ Real electrolyte ⊕ Buried interfaces accessible	⊖ Limited mass transport ⊖ Intermediate probing depth ⊖ Liquid open to vacuum
Graphene covered, holey SiN_x membrane	⊕⊕ Real electrolyte ⊕ Surface sensitive	⊖ Fragile SiNx window and graphene ⊖ Challenging sample preparation ⊖ Small area
PEM without graphene	⊕ Safe in vacuum ⊕ Simple preparation ⊕ Surface sensitive	⊖ Beam sensitive polymer ⊖ Limited mass transport ⊖ No liquid
PEM with graphene (this work)	⊕ Safe in vacuum ⊕ Simple preparation ⊕ Confined liquid comparable to bulk ⊕ Surface sensitive	⊖ Beam sensitive polymer ⊖ Ion transport depends on membrane ⊖ Homogeneity required

strategy to enable soft X-ray spectroscopy of a solid−liquid interface. In the latter case, it is assured that the liquid phase has bulk properties, but the fragile, atomically thin windows pose a high risk to the experimental setup (see Table 1). The fourth approach is the nanofabrication of chips for liquid phase electron microscopy,[9] which tries to diminish the thickness of both the solid and the liquid with success. A more detailed overview of the techniques used in the field of near ambient pressure X-ray photoelectron spectroscopy (NAP-XPS) and environmental electron microscopy can be found in refs 7 and 10 and in refs 11−13, respectively. A summary of approaches comparable to ours are given in Table 1.

Herein, we describe a method that uses a thin graphene window and confined electrolyte. It is safe and simple to use and allows for investigations of the solid−liquid interface. At the heart of our approach is a sample preparation that can be done in any chemical lab (Figure 1): we use solid polymer electrolytes for the transport of ions and water, as others have done before,[14−17] but we cover the polymer membrane or the topping layer of material with graphene (compare Figure 1). The graphene blanket then serves as an evaporation barrier (as shown elsewhere)[4,6,18] and leads to a higher partial pressure of water below it. In previous uses of polymer membranes for similar purposes,[14−17] the catalyst layer faced vacuum and the electrolyte could evaporate. As we will demonstrate in the present article, the graphene barrier helps to retain a thin film of liquid behind graphene at water partial pressures as low well below a millibar. At the same time, graphene provides electrical conductivity[19,20] and is mostly transparent to a wide range of wavelengths[21−23] and slow electrons.[24−26] These benefits allow studies under wet conditions using surface sensitive spectroscopy[27−29] or electron microscopy with the same type of sample.

The material of interest, for example, an electrocatalyst, is sandwiched between the membrane and the graphene blanket (see Figure 1). The thin film of liquid behind graphene is retained. Electrical contact to the material is provided by the graphene cover and ultimately the lid which holds the membrane assembly in place during the measurement. We use a niobium lid coated with boron-doped diamond. It is chemically inert and stable over a wide range of potentials.[30] Ion transport to the deposited material is realized via a polymer electrolyte membrane (PEM), which functions as a solid electrolyte connecting the working electrode with the counter and reference electrode, which are immersed in the bulk liquid (see Figure 1 and the Experimental Section).

In the following we will characterize the sample assembly we advocate. We will start with the homogeneity of the samples and the graphene properties, then proceed to a study of how external parameters influence the wetting, and discuss the ion transport under vacuum, and we will make some remarks about the influence of the beam and about product analysis. In the end, we discuss two scientific showcases to demonstrate the scope of our technique. The first showcase concerns the dissolution of ruthenium under high potentials, and the second visualizes electrodeposition of copper on graphene.

For a convenient recognition of the sample architecture, we will use the short form (0.1 M H_2SO_4)/FAD/IrNPs/SLG to refer to a polymer membrane FAD that is wetted from the back with 0.1 M H_2SO_4 and supports iridium nanoparticles (IrNPs) covered by a single layer of graphene (SLG).

RESULTS AND DISCUSSION

Sample Morphology. The sample assemblies consist of a polymer membrane and a graphene cover. The polymer

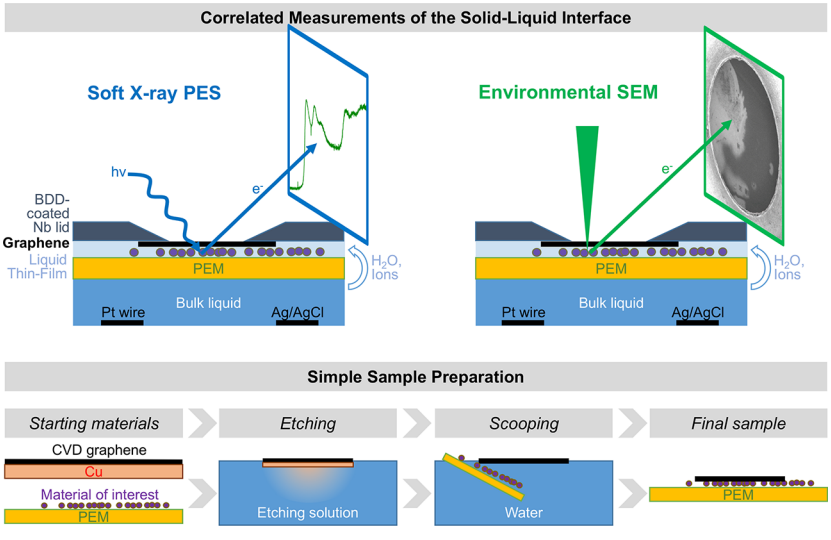

Figure 1. Surface-sensitive investigation of a solid−liquid interface; illustration of the sample architecture and measurement approach (top) as wells as an outline of the sample preparation (bottom).

https://dx.doi.org/10.1021/acsami.0c08379
ACS Appl. Mater. Interfaces 2020, 12, 37680−37692

membranes are usually smooth on the micrometer scale. Nafion 117, for example, has a root-mean-square variation in height of 2.2−3.9 nm, depending on humidity (it becomes smoother when properly hydrated).[31] In this publication we will use Nafion 117 supplied by Ion Power as well as FAD and FKD membranes by Fumatech. The choice of membrane is important in the approach, since it determines the ionic conductivity and can introduce contaminants. More details on the membrane properties, their pretreatments, and their chemical structure can be found in the Experimental Section. CVD graphene from Graphenea is transferred as a single layer of graphene (SLG), a bilayer of graphene (BLG), or a single layer supported by PMMA (SLGp) in a wet chemical process (see the Experimental Section). A representative example of the morphology after transfer is given in Figure 2a,b. These micrographs stem from an environmental scanning electron microscope (ESEM) and show BLG on an FKD membrane. After the mechanical transfer graphene can exhibit tears, but the film is otherwise uninterrupted over hundreds of micrometers (Figure 2a). Sample screening with an optical microscope can, hence, be used to avoid tears in the graphene cover. At larger magnification, wrinkles are evident (Figure 2b), but because of their low density, they will only have a slight impact on the electrical conductivity, the function as a molecular barrier, and a window for radiation and electrons.

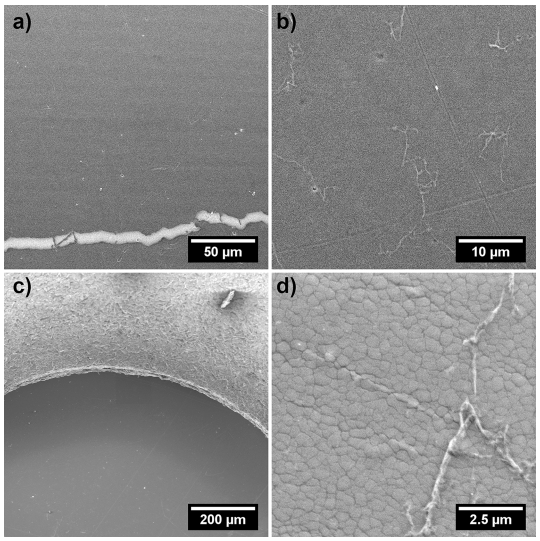

Figure 2. SEM micrographs of (a, b) FKD/BLG and (c, d) FAD/Ru (~4 nm thick)/BLG under ~2 mbar of water. The backsides of the polymer membranes are in contact with aqueous solutions of 50 mM $CuSO_4$ or 0.1 M H_2SO_4, respectively; (c) shows the circular opening of the boron-doped diamond-coated niobium lid.

In most cases an additional layer, that is, an electrocatalyst, is sandwiched between the polymer membrane and graphene. The homogeneity of this layer will depend on the preparation method. We will show results from sputter-deposited films (see the Experimental Section for more details), since they are homogeneous and well-defined, but other techniques like spin-coating, drop-casting, electrodeposition, reductive deposition, or electrophoretic deposition could be applied as well. Figure 2c,d provides SEM micrographs of a sputtered ruthenium film on FAD covered with BLG. The film is homogeneous on a millimeter length scale. However, the films are cracked, as the larger magnification shows (Figure 2d). These cracks likely originate from a mismatch between the metallic layer and the polymer membrane, which swells with increasing humidity.

We can conclude that the present samples are homogeneous on the millimeter length scale. This is important for the following characterization, in which we will make use of Raman and synchrotron-based X-ray spectroscopy to characterize the samples. The spot sizes of these measurements are in the range of a few and one hundred micrometers, respectively (see the Experimental Section). Homogeneity beyond the length scale of the measurement is advisible. It was taken care in this work that the sample assemblies did provide the necessary homogeneity.

Properties of Graphene. Because graphene transfer involves a chemical etching step, the structural and chemical properties of graphene after the transfer need to be assessed. To that end, we provide Raman spectra of SLG and BLG after being transferred with the same method on an oxidized silicon wafer (see Figure 3a). Three typical Raman features of

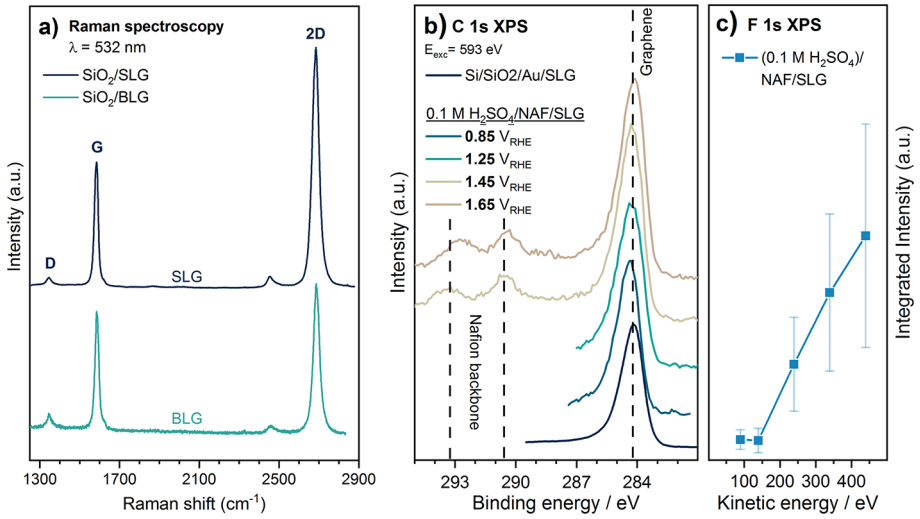

Figure 3. (a) Raman scattering of Si/SiO_2/SLG and Si/SiO_2/BLG at an excitation wavelength of 532 nm. (b) C 1s photoelectron spectra of (0.1 M H_2SO_4)/NAF/SLG at various potentials and of a Si/SiO_2/Au/SLG reference. (c) Integrated F 1s intensity of (0.1 M H_2SO_4)/NAF/SLG at different kinetic energies.

https://dx.doi.org/10.1021/acsami.0c08379
ACS Appl. Mater. Interfaces 2020, 12, 37680−37692

graphene will be used for the characterization: first, a defect-induced peak of zone-boundary phonons (D) at ∼1350 cm^{-1}, second, the vibrational excitation of a doubly degenerate zone center E_{2g} mode (G) at ∼1580 cm^{-1}, and third, a peak related to the second order of zone-boundary phonons (2D).[32] The intensity ratio of D to G (I_D/I_G) has been used to evaluate the degree of disorder in graphene.[32,33] The SLG and BLG both show an I_D/I_G ratio ∼0.1 after transfer. Together with a sharp G peak (the full width at half-maximum is about 20 cm^{-1}), this ratio is indicative of a good structural integrity. The wet transfer method, hence, provides graphene cover layers. A more detailed analysis of the Raman spectroscopy and a comparison to PMMA-assisted graphene transfer process is provided in the Supporting Information.

Because the morphological and structural integrity of the graphene layer after transfer is now shown, we will discuss how this graphene layer assists the goal of measuring a biased solid−liquid interface. It fulfills three functions. First, it is used as a current collector and support, second, it serves as a window for radiation and electrons, and, third, it acts as an evaporation barrier for water.

To fulfill its first function, graphene needs to be in good contact to the lid (see Figure 1) and provide conductivity over the range of the circular front plate opening, which is 1.5 mm in diameter. This property is demonstrated by X-ray photoelectron spectroscopy of the C 1s spectrum at several potentials and measurement positions (see Figure 3b). The main peak of the C 1s spectrum is originating from graphene, as the black reference spectrum of SLG on gold at the bottom of Figure 3b indicates. Graphene's peak position is expected to be constant with potential if the working electrode, that is, graphene, is conductive and grounded to the electron analyzer, which is why it was used as standard configuration, except in Figure 3b (see the Experimental Section for more details). Figure 3b shows the C 1s spectrum at different potentials and measurement positions (each measurement is ∼0.2 mm apart). The variation of the peak position in Figure 3b is <±0.2 eV and is probably composed of an uncertainty in the excitation energy, which is ±0.1 eV (see the Experimental Section), the work function of the sample, and incomplete screening of the surface potential of graphene.[34] The latter is caused by quantum capacity effects.

The second function of graphene is to be a window for incoming and outgoing radiation and slow electrons. It has indeed been shown earlier that graphene is transparent for most radiation[21−23] and slow electrons.[25,26,35] Especially the latter is crucial for surface sensitive photoelectron spectroscopy used in this work. We determined the minimal kinetic energy of photoelectrons required to pass graphene by depth profiling of the F 1s photoelectron spectrum in (0.1 M H_2SO_4)/Nafion/SLG. The F 1s photoelectron signal originates from the tetrafluoroethylene backbone of the Nafion membrane below graphene, so the photoelectrons originating from Nafion have to (at least) pass SLG. Figure 3c shows the integrated F 1s intensities for kinetic energies of the electrons ranging from 90 to 440 eV. The corrected intensity of the F 1s (see the Experimental Section) signal is constant below 150 eV and continuously increases above that value. This means that electrons with a kinetic energy of higher than ∼200 eV are already fast enough to escape from the (hydrated) polymer membrane through SLG. This is well in line with the result obtained from free-standing BLG, in which the kinetic energy must be higher than 400 eV.[36] The probing depth expected for electrons with a kinetic energy of 200 eV is ∼1 nm. In fact, such a kinetic energy is close to the minimum effective attenuation length in water,[37] making our technique well suited for extremely surface sensitive measurements of the solid−liquid interface.

Wetting. It has now been shown that the covering graphene layer can serve as a current collector and as a window for radiation and electrons faster than 200 eV, but we have not yet shown that there is a liquid layer between the membrane and graphene. In the following, we will provide evidence from O K-edge absorption that there is a layer of confined water that is similar to bulk water. We also systematically studied whether the partial pressure of water in the gas phase, the number of graphene layers, and the contact of the polymer to bulk water influence the wetting.

We start the evaluation of wetting with the comparison of two O K-edge absorption spectra (Figure 4a). Both spectra

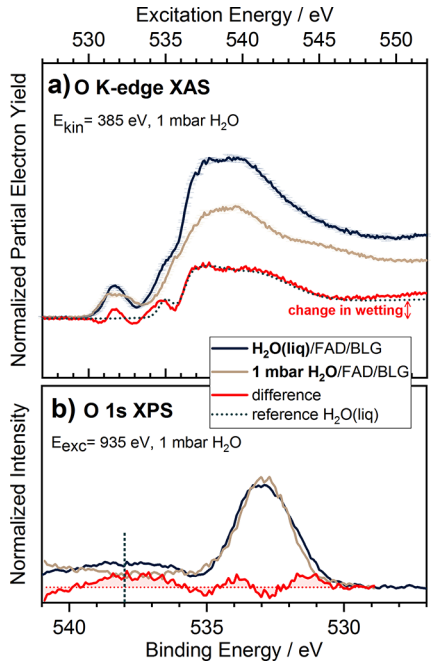

Figure 4. (a) O K-edge absorption and (b) O 1s PES of (1 mbar of H_2O)/FAD/BLG and H_2O(liq)/FAD/BLG in 1 mbar of H_2O, their difference, and a comparison to a liquid water reference are shown; the reference absorption spectrum of liquid water was provided by Schreck et al.[38]

show an FAD membrane with a BLG cover at 1 mbar of H_2O, but only one of the samples is wetted with bulk water from the backside. The two spectra are normalized to the integrated pre-edge intensity at ∼532 eV, which originates from the polymer membrane and carbonaceous species, and subtracted from each other (see the Experimental Section for more details and reasoning). The difference spectrum presented in red shows a clear fingerprint of liquid water. This becomes especially apparent when comparing to a reference spectrum of liquid water measured in transmission (shown as a dotted line; used with permission from Schreck and Wernet et al.[38]). This thin film of liquid is trapped between the polymer membrane and graphene. These boundaries are expected to disturb the local hydrogen bonding and hence lead to an enhancement of single-donor hydrogen bonding. As a consequence, the pre- and main-edge features at 535 and 537.5 eV originating from

https://dx.doi.org/10.1021/acsami.0c08379
ACS Appl. Mater. Interfaces 2020, 12, 37680−37692

single-donor hydrogen bonding should be enhanced relative to the postedge, which can be assigned to water in a double-donor hydrogen-bonding network.[39,40] Strongly confined liquid indeed show a strong enhancement of the main-edge contribution.[41] However, we cannot detect a significant difference from bulk liquid water with our method. This means that the liquid is thick enough to not show altered hydrogen bonding. According to Cicero et al.,[42] water confined by graphene adapts bulk properties within 5 Å from the interface. This suggests that the liquid thin film using this method needs to exceed 10 Å. This is sensible considering that the height variation of polymer membranes is in the order of a few nanometers.[31] These voids are covered by graphene and could be filled with liquid as long as graphene seals.

The XPS signal of the O 1s level (see Figure 4b) also provides evidence for a phase similar to bulk water. To extract the changes in the O 1s spectra that are related to an improved wetting, we scaled the integrated intensity of the XPS spectrum by the edge jump of the respective O K-edge (Figure 4a). This procedure is correct if the integrated intensity of XPS and the edge jump of XAS are proportional to the number of species in the probed volume. The latter is expected to be larger for the partial electron yield of the XAS measurement, leading to an underestimation of the liquid contribution in the XPS difference spectrum. The scaled O 1s XP spectra in the dry and the wet state and their difference are given in Figure 4b. A feature at ~538 eV appears in the difference, indicating bulk water.[37] The main peak also shows slight deviations between the dry and the wet state, but they could be caused by a different peak width or a different distribution of carbonaceous species.

To describe how the water backpressure, the number of graphene layers, and bulk water behind the PEM membrane influence the liquid thin film, we varied these parameters systemically. By comparing two different conditions at a time (as in Figure 4a), we found that bulk water behind the polymer membrane had the largest impact on the level of wetting. Water backpressure had a weak effect on wetting, unless the samples were in contact with liquid water from the back. Samples covered with SLG and BLG behaved similarly. For the complete discussion, we refer to the Supporting Information.

The study of wetting showed that a liquid thin film is formed between graphene and a polymer membrane. A close contact between graphene and the polymer membrane is, however, not strictly necessary to create wet conditions. It can also form if a layer of catalyst is sandwiched between the two (compare Figure S4), suggesting that graphene's role as an evaporation barrier is mostly determining the wetting, not the interaction between graphene and the material below it.

Ion Transport. After verifying the wet conditions below the graphene layer, we turn to the ion transport necessary for most processes of interest at the liquid–solid interface. Crucial for the ion transport is the polymer membrane, which serves as a solid electrolyte. An appealing side effect of using solid electrolytes is that the choice of membrane can selectively allow some ions to pass and block others. Among the membranes we used in our studies, there is Nafion (NAF) conducting water and protons, the FAD membrane conducting anions in addition, and the FKD membrane, which conducts water and cations. The FAD membrane is therefore suited for aqueous acidic electrolytes, the FKD can be used for solvated metal ions, and Nafion can be used to study a given electrolyte without the counterions and only protons.

As a summarizing example of ion transport in our approach we chose the diffusion of the electrolyte H_2SO_4 across an FAD membrane. The experiment is equivalent to the wetting experiment in Figure 4a,b, but the sample is wetted with 0.1 M H_2SO_4 instead of pure water. The potential is controlled at 0.25 V_{RHE}. The resulting difference spectra of the O K-edge absorption (Figure 5a) and O 1s XP spectra (Figure 5b)

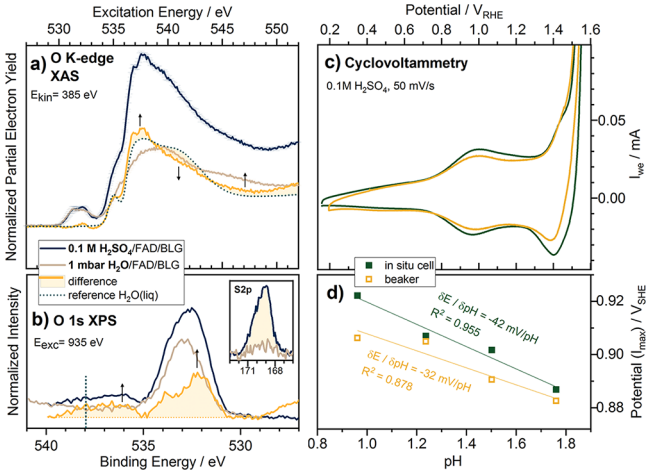

Figure 5. (a) and (b) are analogous to Figures 4a and 4b but recorded on (0.1 M H_2SO_4)/FAD/BLG at 0.25 V_{RHE}. (c) Cyclovoltammogram at 50 mV/s and (d) the potential shift of the oxidation wave at ~1 V_{RHE} with varying pH of (0.1 M H_2SO_4)/FAD/IrNPs/SLG and HOPG/IrNPs/(0.1 M H_2SO_4).

change drastically. A liquid layer is still present, as the differences of the O K-edge absorption exhibit the features of liquid water, but the O K-edge absorption intensities at about 537 and 547 eV increased, while the intensity around 541 eV decreased when compared to pure water (Figure 4a,b). This behavior is in good agreement with the study of Niskanen et al.,[43] in which the authors report very similar changes in the O K-edge absorption of sulfuric acid at different concentrations measured by inelastic X-ray scattering. The XP difference spectrum has a feature slightly above 532 eV, in addition to the one at about 538 eV. The latter originates from water, while the former fits well to the reported O 1s binding energy of sulfuric acid at low temperatures (532.3 eV).[44] The S 2p contribution at 169 eV shows that sulfate ions can indeed pass (inset of Figure 5b). It is also noticeable that the contribution at ~538 eV is not symmetric due to an increase at ~536 eV.

The observed changes in the O K-edge difference spectra between 0.1 M H_2SO_4 sulfuric acid and pure water in this study are comparable to the changes observed by Niskanen et al.[43] for 4–8 M H_2SO_4 and pure water, despite the much lower concentration in the present experiment. The reason can be found in the probing depth. In this study we used the kinetic energy of roughly 400 eV, which just exceeds the energy needed to pass the two layers of graphene. In contrast, X-ray scattering used in the study of Niskanen is a bulk sensitive method. That means the solid–liquid interface between sulfuric acid and graphene is in comparison to bulk sulfuric acid, enriched with sulfate ions. The dependency of this effect on the applied potential was not investigated in the present publication.

An alternative explanation is that this local pH effect is enhanced in the liquid thin film when compared to bulk

https://dx.doi.org/10.1021/acsami.0c08379
ACS Appl. Mater. Interfaces 2020, 12, 37680–37692

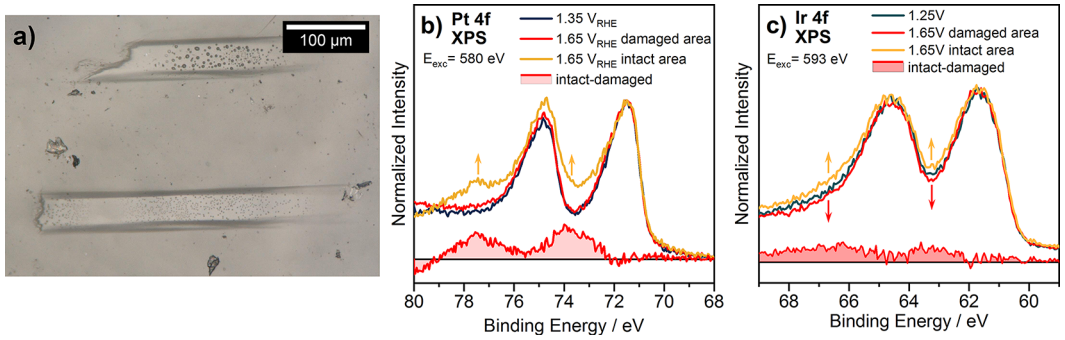

Figure 6. Interaction with a soft X-ray beam: (a) image obtained from an optical microscope of Nafion/Ir NPs/SLG after intensive beam exposure, (b) operando Pt 4f XP spectra of 0.1 M H_2SO_4/Nafion/Pt/SLG, and (c) operando Ir 4f XP spectra of 0.1 M H_2SO_4/Nafion/Ir NPs/SLG recorded at intact and damaged measurement positions; their difference is shown in red.

electrolyte. We thus compared to an experiment in bulk electrolyte by depositing Ir nanoparticles on highly oriented pyrolytic graphene (HOPG) and recording cyclovoltagramms (CVs) in bulk electrolyte and in the in-situ setup at varying concentrations of H_2SO_4. Two exemplifying CVs using 0.1 M H_2SO_4 are given in Figure 5c. Their features and general shape match and differ only slightly. The most prominent oxidation feature at ~1 V_{RHE}, which is characteristic for iridium (hydr)oxides and known to shift with pH,[45,46] was then used to track the pH shift. The results are shown in Figure 5d. Both the beaker experiment and the in-situ cell behave similarly, though there are differences in the slope of the linear fits. We, therefore, cannot exclude that the local pH at the graphene–electrolyte interface in our sample assembly is different from what it would have been in bulk electrolyte. However, the difference is much smaller than 1 pH unit based on the potential shift between the curves.

We have seen that the sample architecture we suggest can provide a thin film of sulfuric acid containing water, protons, and sulfate ions between a polymer membrane and graphene. In two further examples, we can show that a proper transport of ions in this approach is not limited to the example of sulfuric acid but can indeed be extended to other solutions. First, Figure S5 shows that the addition of chloride ions to 0.1 M H_2SO_4 leads to a strong increase in the Cl 2p signal on the side of graphene. Second, we demonstrate that a copper sulfate solution behind the membrane allows copper deposition on graphene or its dissolution in a reversible fashion (compare "Showcase 2").

Interaction with an X-ray Beam. Soft X-rays or fast electrons interact with the polymer membrane, which then suffers from radiation damage. Examples are given in Figure 6. Figure 6a shows the image of a Nafion membrane after ~20 min of beam exposure at the ISISS beamline, which equates to a beam dose of about 0.3 Gy assuming the beam is completely absorbed (see the Experimental Section). The damage is obvious in the elongated rectangles, which roughly resemble the shape of the beam spot at the ISISS beamline at 111 μm slit size. Although the exact route of damage is unknown, the bubbles in Figure 6a point toward radiolysis of the liquid and the polymer.

The induced damage leads to a limited charge transport through the membrane. The evidence is provided in Figure 6b,c. Both show XP spectra of a metal core level in 0.1 M H_2SO_4 before and after an oxidation step. The oxidized state was recorded in two areas: an area damaged by the beam and a fresh, intact area. In the case of platinum (Figure 6b), the intact area, which was only irradiated during data collection for ~80 s, shows the expected oxidation to Pt^{4+}, leading to a doublet at ~73.5 and ~77.5 eV.[16,28] However, the area irradiated for about 20 min shows almost no change after the oxidation step. A similar effect can be seen with oxidized iridium nanoparticles on Nafion (Figure 6c). By increasing the potential from 1.25 to 1.65 V_{RHE}, it is expected that the spectrum broadens toward high binding energies.[8,27] This is not the case for the measurement on the same spot, after 15 min of beam exposure, but is true for the fresh spot, which was only irradiated during the data acquisition of 150 s. Consequently, the change caused by the applied bias is slow or hindered when the area is damaged by the beam. This is likely to be caused by a limited mass transport after damage. A loss of electrical conductivity is unlikely since the binding energy of the metal is stable with potential, even after damage. We recommend not to exceed a beam dose of ~0.1 Gy for a reliable result (see the Experimental Section).

Interaction with an Electron Beam. In the case of electron microscopy, the beam dose can be regulated by acceleration voltage, emission current, and magnification, but radiolysis of liquids caused by an electron beam is a known phenomenon for SEM[47,48] and TEM.[12,13,49] We optimized the acceleration voltage and the magnification for the operando experiments in the environmental scanning electron microscope. To demonstrate the damage caused by an electron beam, copper deposition in 50 mM $CuSO_4$/FKD/BLG is chosen as an example. The upper micrographs (Figure 7a–c) show snapshots of copper dissolution and deposition at small magnification. The respective potentials and electrochemical currents are given in Figure 7d. The pixel arrays of a damaged area (indicated in Figure 7b) and an intact region slightly above it were analyzed for the average pixel intensity, which is given in Figure 7e. Respective snapshots (Figure 7a–c) are indicated in Figure 7e. It becomes evident that a change in the mean brightness is initiated by electrochemical currents. Anodic potentials and positive currents lead to dissolution and a decrease in the mean brightness while cathodic potentials and negative currents increase the mean brightness. This effect is, however, much more pronounced in the intact region compared to the damaged region, pointing toward a strongly limited mass transport after intense exposure to the electron beam.

As hinted in the section about the morphology of the sample, it becomes more evident now why it is important to provide homogeneity on the length scale of the respective measurement. After investigation of one spot at a given

https://dx.doi.org/10.1021/acsami.0c08379
ACS Appl. Mater. Interfaces 2020, 12, 37680–37692

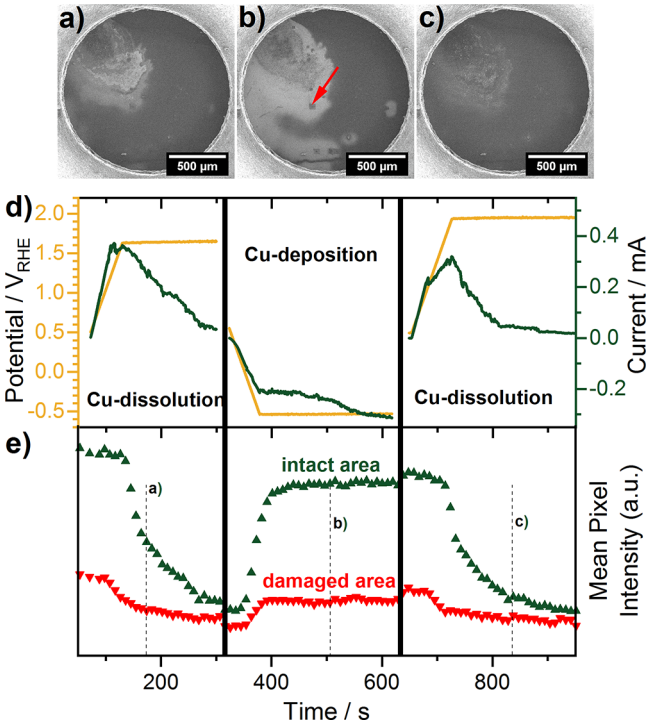

Figure 7. Operando SEM micrographs of (50 mM $CuSO_4$)/FKD/BLG at (a) 1.65 V_{RHE}, (b) −0.55 V_{RHE}, and (c) 1.95 V_{RHE} with (d) the respective potential and current and (e) the mean pixel intensity of a damaged area (dark rectangle indicated in part b by a red arrow) and of a pixel array with the same size slightly above the damaged area.

condition, the mass transport on that position will be affected. It is therefore needed to change the position for the next measurement at a new condition. In such an experiment, homogeneity is the prerequisite for a reliable comparison of the findings at different experimental conditions.

Product Analysis. For operando investigations of electrocatalysts, product analysis is crucial. In the in-situ technique suggested here, it is possible to detect gaseous products, evolving at the working electrode. In our setup for in-situ X-ray spectroscopy, for example, a mass spectrometer behind a leak valve was used for the analysis of the gas atmosphere. With this method, an oxygen evolution of 2 nmol/s is well above the detection limit (see Figure S6).

Two Showcases of in-Situ Electrochemistry. We chose two showcases to illustrate the properties and scope of the in-situ setup described above. First, we show the dissolution of ruthenium at anodic potentials with in-situ electron microscopy and X-ray spectroscopy. Second, the same two techniques are used to track copper deposition on the graphene cover. In addition to the showcases in the present publication, recently published articles show the electrochemical oxidation of iridium[27] or platinum nanoparticles[28] under acidic conditions.

Showcase 1. The first showcase is the dissolution of ruthenium under anodic potentials. The sample assembly is an FAD membrane covered with a thin layer of sputtered ruthenium metal and SLG. It was activated with 20 cycles between 0 and 1.15 V_{RHE} at 50 mV/s. The O K-edge absorption of the activated layer shows few signs of oxidation (Figure 8a), except for a feature slightly above 531 eV, which could be related to ruthenium hydroxides. Applying an oxidative potential (e.g., 1.25 V_{RHE}) instantly leads to an

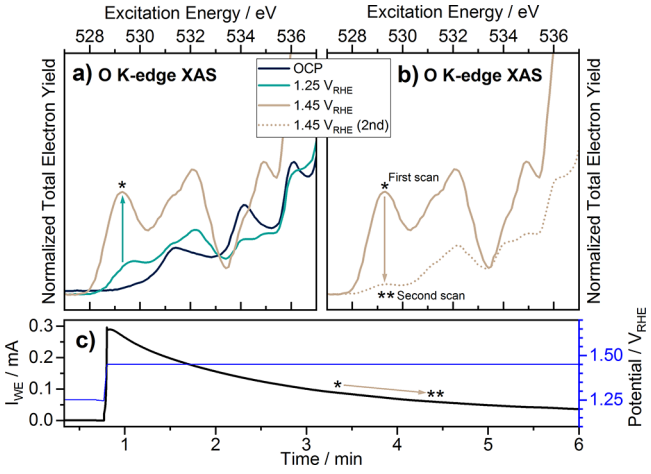

Figure 8. Oxidation of (0.1 M H_2SO_4)/FAD/Ru(4 nm thick)/SLG: (a) operando O K-edge absorption at three potentials and (b) two consecutive spectra at 1.45 V_{RHE}; (c) the respective potential and currents during spectroscopy.

absorption white line at 529 eV (see Figure 8a), which is known for oxidized ruthenium. A further increase of the potential from 1.25 to 1.45 V_{RHE} leads to a more intense white line. This effect, however, does not sustain for long. The signal from oxidized ruthenium is strongly diminished in a consecutive spectrum about 2 min later (Figure 8b). The current of the working electrode is quickly degrading (Figure 8c).

An explanation for this behavior is well illustrated by an analogue study in the environmental SEM. We used the same type of sample as in the previous experiment (0.1 M H_2SO_4/FAD/Ru/SLG) but partially covered with SLG. We activated this assembly by 50 voltammetric cycles between 0.05 and 1.25 V_{RHE} at a rate of 50 mV/s. The micrograph recorded after this treatment shows a layer of ruthenium traversed by cracks. The Ru layer is homogeneously distributed and partially covered with graphene (Figure 9a). After polarization of this layer to 1.45 V_{RHE} for 25 min and 1.55 V_{RHE} for 4 min, another micrograph was recorded (Figure 9b). The bright contrast of the ruthenium layer disappeared in the areas covered with graphene. However, in the areas without a graphene cover, the ruthenium layer appears unchanged by the treatment. This demonstrates the importance of graphene in this arrangement.

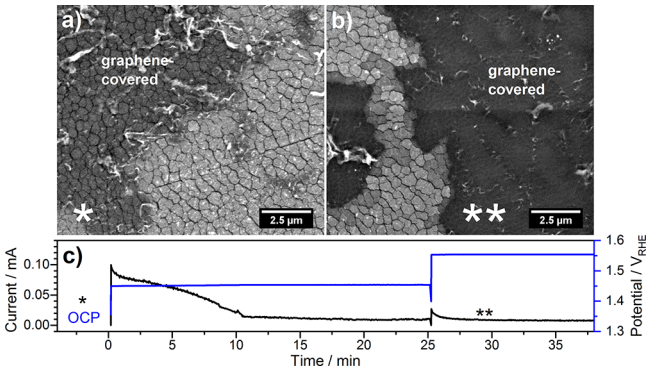

Figure 9. Oxidation of (0.1 M H_2SO_4)/FAD/Ru(4 nm thick)/SLG; operando SEM micrographs of (a) before and (b) after Ru dissolution in the graphene-covered areas; (c) the respective potential and current during the experiment.

https://dx.doi.org/10.1021/acsami.0c08379
ACS Appl. Mater. Interfaces 2020, 12, 37680−37692

By providing conductivity and a wetted environment, electrochemical processes and significant mass transport can occur at pressures below 1 mbar (darker areas in Figure 9). Without graphene, these processes are hindered and sluggish (bright areas in Figure 9).

Showcase 2. The second showcase is the electrodeposition of copper. To enable the transport of Cu cations, we used the FKD membrane and covered it with a bilayer of graphene (BLG). We introduced an aqueous solution of $CuSO_4$ (50 mM) and deposited copper particles at potentials below −1.3 V_{RHE}. The result obtained in the environmental SEM can be seen in Figure 10a. The copper particles appear bright, and

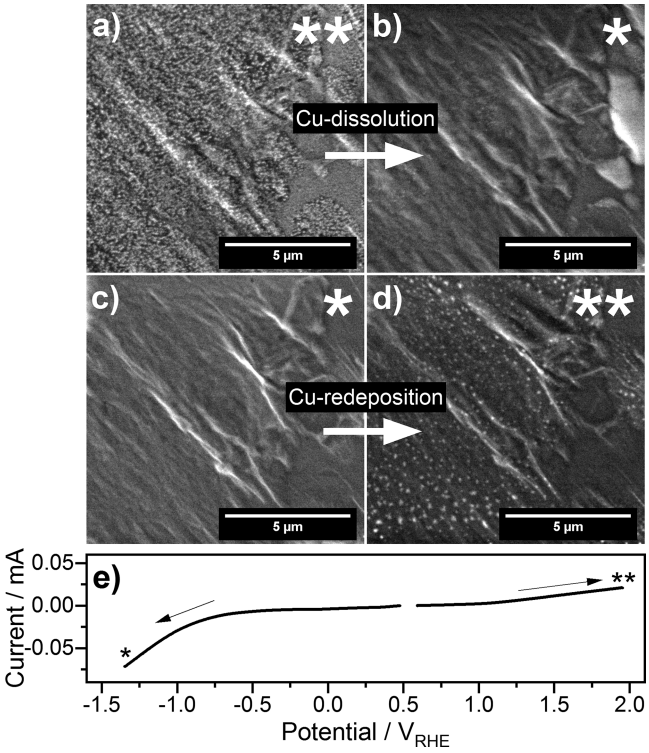

Figure 10. Dissolution and redeposition of Cu; operando SEM micrographs of (50 mM $CuSO_4$)/FKD/BLG at (a, d) −1.35 V_{RHE} and (b, c) 1.95 V_{RHE}; (e) the respective linear sweep voltammetries.

they are stable at potentials <1 V_{RHE} (see also Figure 7). The particles are some tens of nanometers wide. If the potential was increased to 1.8 V_{RHE}, the particles dissolve again (see Figure 10b). The redeposition of Cu at −1.3 V_{RHE} (from Figure 10c,d) in the same area results in the growth of bright, but fewer, particles. This hysteresis is likely caused by the damage of the membrane with the electron beam slowing down the mass transport significantly (see also section about beam interaction).

The same process can be observed with operando X-ray spectroscopy (Figure 11). Again, an aqueous solution of $CuSO_4$ is provided behind an FKD membrane. Figure 11a shows the Cu L-edge spectrum before deposition. A broad background feature between 935 and 940 eV is observed. As soon as copper is deposited at −1.15 V_{RHE}, characteristic absorption resonances of metallic copper[50] appear at 933.7, 937.9, and 941.7 eV.

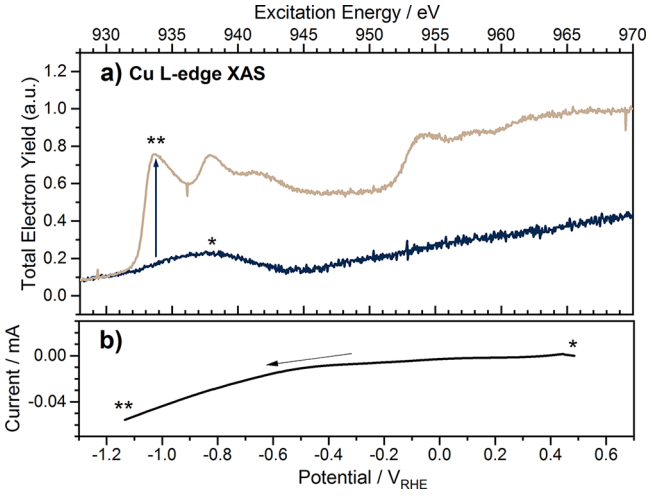

Figure 11. Deposition of Cu: (a) operando Cu L-edges of (50 mM $CuSO_4$)/FKD/BLG before (dark blue) and after (beige) Cu deposition at −1.15 V_{RHE}; (b) the respective linear sweep voltammetry.

CONCLUSION

We demonstrated a way to investigate the solid−liquid interface by using a sample preparation method that can be done in any chemical lab. The key to our approach is the sample assembly, in which an electrocatalyst is sandwiched between a (bi)layer of graphene and a permeable membrane in contact with bulk electrolyte. Water and ions pass from the bulk electrolyte through the membrane and form a liquid thin film beneath the graphene blanket. This liquid film is stable at pressures in the mbar range and was found to be similar to bulk liquid. Furthermore, photoelectrons with kinetic energies down to 200 eV can be detected through the liquid thin film and the graphene window, which allows for extremely interface sensitive measurements of solid−liquid interfaces. We show this ability with X-ray photoelectron spectroscopy and scanning electron microscopy—two powerful techniques which are still rarely used for the study of the solid−liquid interface or electrochemical processes due to technical hurdles. In two showcases, we performed operando X-ray spectroscopy and operando SEM on the same sample types and could follow electrochemical dissolution of ruthenium and the electrodeposition of metallic copper under wet conditions.

EXPERIMENTAL SECTION

Sample Preparation. We used the following polymer membranes: FAD55 (FAD) and FKD provided by Fumatech and Nafion 117 (Nafion) provided by Sigma-Aldrich (see Table 2 for their basic properties). Nafion is an ionomer produced by the copolymerization of perfluorinated vinyl ether and tetrafluoroethylene.[51] Both membranes by Fumatech are functionalized polyarylenes, while the FAD membrane is a quaternized poly(phenyl oxide) and the FKD membrane is a sulfonated poly(ether ketone). All of them were cut to circular disks of 11 mm in diameter but activated and stored them in different ways. FAD disks were soaked for at least 3 days in 0.5 M Na_2SO_4 solution to exchange bromide counterions for sulfate ions. The solution was exchanged several times during treatment. Residual bromide remains.[27,28] Samples including FAD membranes were stored in the soaking solution until use. FKD membranes were not activated and stored dry. Contamination originating from the FKD membrane was not detected. Nafion disks were rid of carbonaceous contamination for 2 h at 80 °C in 3% H_2O_2 solution and another 2 h

https://dx.doi.org/10.1021/acsami.0c08379
ACS Appl. Mater. Interfaces 2020, 12, 37680−37692

Table 2. Properties of the Polymer Membranes as Specified by the Supplier

	Nafion 117	FAD	FKD
thickness (μm)	183	50−60	68−77
pH range		1−9	1−14
type of exchange	H^+	anion/H^+	cation/OH^-
selectivity (%)		85[a]	>95[a]
H^+/OH^- conductivity or transfer rate	>0.1[b] S cm^{-1}	8000−10000[c] μmol min^{-1} cm^{-2}	<250[c] μmol min^{-1} cm^{-2}

[a]Measured in concentration cell with 0.1/0.5 mol kg^{-1} KCl at T = 25 °C [b]Conditioned at 100 °C, measured by impedance at 25 °C.[52] [c]From pH potential measurement in concentration cell with 0.1 M HCl/0.1 M NaCl at T = 25 °C.

at the same temperature in 0.5 M H_2SO_4. Samples prepared from Nafion were stored in a dry state until used.

The material of interest was deposited by the DC magnetron sputter coater 208HR by Cressington (Watford, UK). The sputtering process was always performed at 0.1 mbar argon atmosphere and with a sputtering current of 40 mA. The thickness was controlled by sputtering time. The iridium sputter target was provided by Elektronen-Optik Service GmbH (Dortmund, Germany) and the ruthenium target by ChemPur (Karlsruhe, Germany).

Graphene was transferred in a wet chemical method. Graphene on copper foil was purchased from Graphenea in the form of a single layer, a PMMA-coated single layer, or a double layer. They were stored as shipped or in the glovebox after being opened. Graphene on copper was cut into rectangular pieces of about 4 mm with a scissors, and the supporting copper foil was etched in an aqueous solution of 40 g/L $(NH_4)_2S_2O_8$ overnight. After the solution was exchanged to pure water, the floating graphene layer, which is visible against a white background, was transferred from below onto the polymer membrane disks (see Figure 12). Alternatively, the layer can be picked up from the top, as illustrated in Figure 12 (method 3). Residues of PMMA after transfer were removed dropwise with acetone (method 2). The samples were dried on air at room temperature after transfer. We assured proper placement of graphene by visual inspection. The quality of graphene was examined with SEM. If the relative placement of graphene on the polymer membrane is relevant, the assembly can be cut after transfer.

Raman Spectroscopy. Raman spectra were collected by using a confocal Raman microscope (TriVista TR557 spectrometer, S&I GmbH) equipped with a 532 nm excitation laser (EL = 2.33 eV) which was focused on the samples using a 50× objective. The measurement areas were chosen randomly in the relevant sample area. Special care has been taken to avoid laser-induced change or damage. Raman scattering was collected by using laser powers between 0.1 and 10 mW for 20−1200 s. No significant change of the spectral features was observed over these times.

In-Situ X-ray Spectroscopy. All experiments were performed at the ISISS beamline at BESSY II in Berlin. An exception is the study of relative wetting, which was performed at the UE56-2 PGM1 beamline, also at BESSY II. Both use differentially pumped analyzers designed for pressures in the millibar range. The same measurement chamber was used at the two beamlines. The chamber, including the manipulator, was designed for the purpose of electrochemical in-situ studies and has been shown earlier.[36] The cell design used in this publication is shown in Figure 13a. The main body made of PEEK houses the tip of the reference electrode and the counter electrode in the form of a curled platinum wire (see Figure 13a,c). Both are in a stream of liquid provided through PEEK tubing. The polymer membrane is mounted on the front, supported by a grid, and sealed by an O-ring. The pressure from the top is provided by a lid made of glassy carbon or niobium with a boron-doped diamond coating. A photograph of a mounted cell is given in Figure 13b, and a technical drawing of the cross section is shown in Figure 13c.

During the experiments, potentials were referenced to the Ag/AgCl electrode DRIREF-2SH, which was stored in saturated KCl solution between experiments. The working electrode including graphene and the cover lid was grounded to the hemispherical analyzer. An exception is data of Figure 3b, in which the electrolyte was grounded, and the recorded signal was shifted by the applied potential. The latter procedure therefore includes changes in the work function of the sample. All potentials were corrected for pH and iR, but we neglected possible deviations caused by incomplete screening of the surface charge,[34] whose magnitude was not measured. For reasons of the latter, the significant figures of the calculated potentials against the reversible hydrogen electrode (RHE) might not be adequate. During the experiment the pressure ranged from 5.0×10^{-2} to 1.5×10^{-1} mbar. In the case of pressure control, additional water vapor was added to the chamber via a low pressure-difference mass flow controller by Bronkhorst (Ruurlo, Netherlands), and a PID-controlled, pressure-regulating valve by Pfeiffer Vacuum GmbH (Asslar, Germany) was used to keep the pressure in the chamber constant.

The dose of the beam was calculated by dividing the total energy per time by the mass of the membrane in the area of the beam at a given thickness.[53] We assumed full absorption of the beam. For the example of a Nafion 117 membrane (183 μm thick) irradiated at the ISISS beamline with an excitation energy of 800 eV (flux(800 eV) ≈ 1×10^{11} photons/s) and a beam size of 150 × 100 μm, we obtain

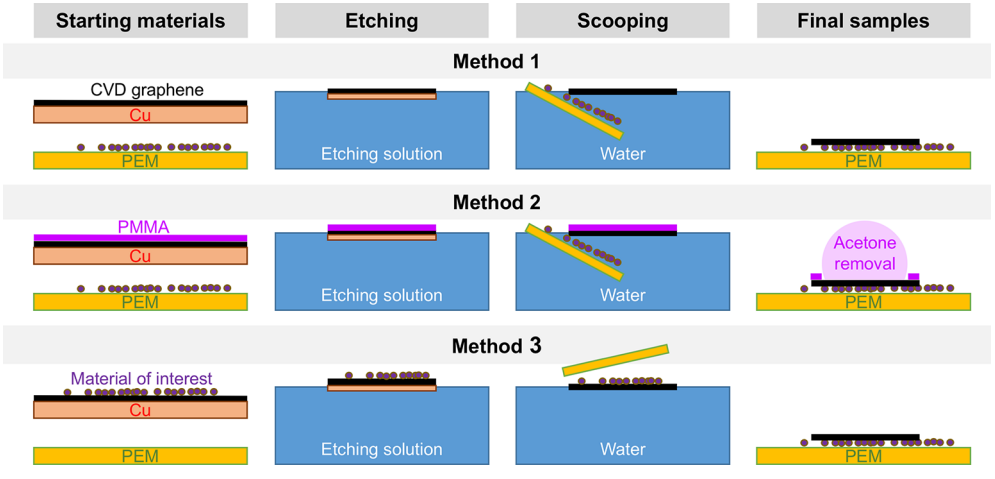

Figure 12. Schematics of three sample preparation methods: wet chemical transfer from below (method 1), PMMA-assisted transfer from below (method 2), and a transfer from above (method 3).

https://dx.doi.org/10.1021/acsami.0c08379
ACS Appl. Mater. Interfaces 2020, 12, 37680−37692

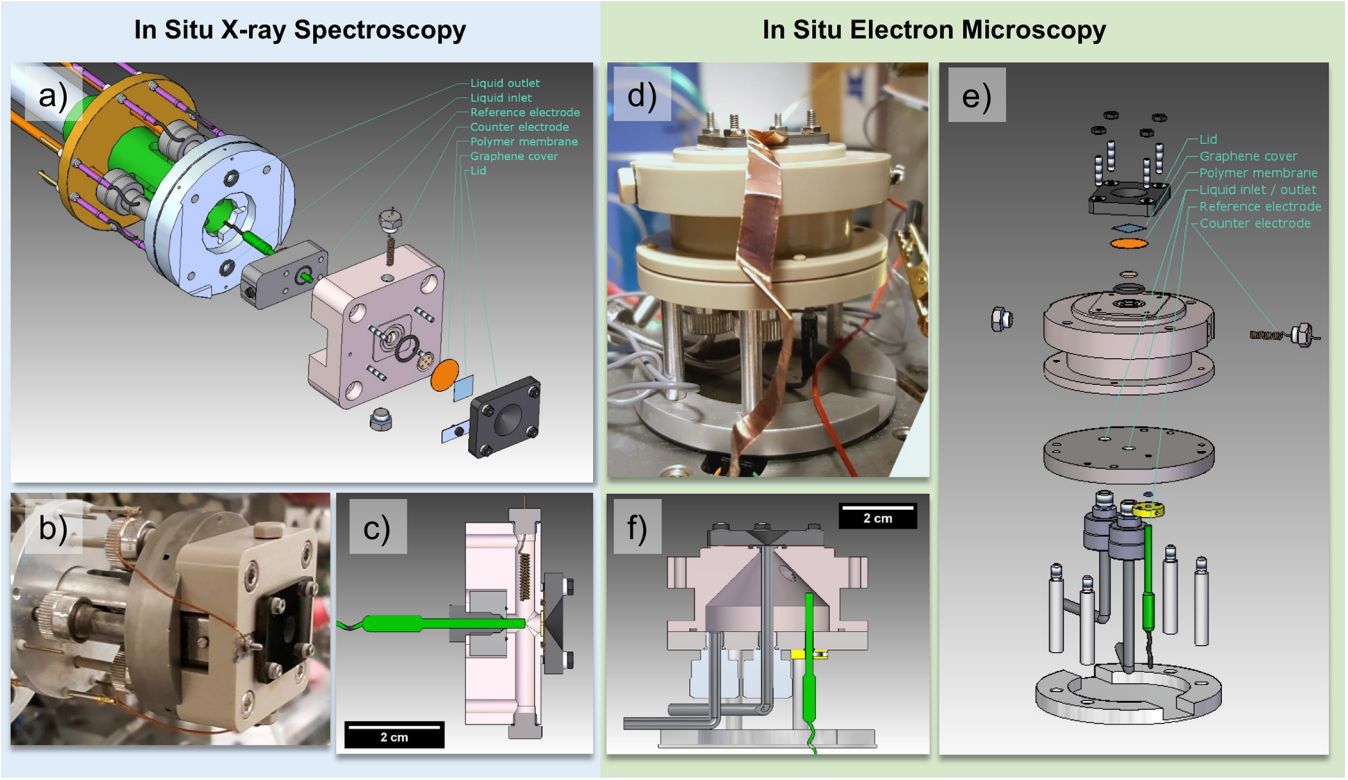

Figure 13. Cell for in-situ spectroscopy with (a) exploded view, (b) photograph of a mounted cell, and (c) cross section; cell for in-situ electron microscopy with (d) a photograph of the mounted cell, (e) the exploded view, and (f) the cross section.

$$\text{dose/s} = \frac{\text{energy/s}}{\text{mass}} = \frac{1 \times 10^{11}\ \text{photons/s} \times 800\ \text{eV/photon}}{2\ \mu\text{g}/\mu\text{m}^3 \times 1.5 \times 10^4\ \mu\text{m}^2 \times 183\ \mu\text{m}}$$
$$\approx 1.5 \times 10^9 \frac{\text{MeV}}{\text{s}\cdot\text{kg}} = 0.24\ \text{mGy/s} \quad (1)$$

where we assumed monochromized radiation and neglected higher-order contributions to the beam. A measurement of 3 min would under the stated assumptions result in ∼0.04 Gy. We recommend to avoid beam doses of above >0.1 Gy for reliable results. This recommendation is based on experience at the ISISS beamline investigating OER catalysts under acidic and basic conditions as well as copper deposition. After about 7 min of measurements at the ISISS beamline, the measurement spot was notably affected by radiation damage.

In-Situ Electron Microscopy. Environmental electron microscopy was performed on a modified scanning electron microscope (SEM) FEI Quanta 200 FEG. All measurements were performed at an acceleration voltage of 5 kV. The gas mixture was composed of Ar, dosed with 1 mL/min, and H_2O leaking from the in-situ cell. The operating pressure during experiments was around 0.2 mbar. A photograph of the home-built in-situ cell is shown in Figure 13d and an exploded view in Figure 13e. The cell provides the same sample surrounding as the in-situ cell for X-ray spectroscopy described above. The counter and reference electrodes are chosen as described above. However, the reference and counter electrodes are placed differently, and the electrolyte exchange is realized in another way: the cell is filled from below, while the outlet is a tube reaching just below the membrane. Reference and counter electrodes are immersed in the liquid but have different spacing to the working electrode. A cross section is provided in Figure 13f.

Data Analysis. The O K-edge absorption was calibrated to the 3p Rydberg state of gas phase water at 537.25 eV.[40] The excitation energy in the case of X-ray photoelectron spectroscopy was calibrated with tables created by using the Fermi edge of a gold foil during the same week. The uncertainty using this method is ∼0.1 eV for the beamlines we used.

A self-made Python-based script was used to process the O K-edge absorption spectra. It accounts for energy calibration, the ring current of the synchrotron, and the flux of the beamline. It also normalizes to zero and one at given excitation energies. Furthermore, it compensates for gas phase attenuation of the X-rays as in ref 54. The flux reference was recorded on a gold foil free of oxygen.

Integrated intensities of F 1s (Figure 3c) were obtained by subtracting a Shirley background and integrating the total area. The results were corrected for cross section and an averaged asymmetry parameter, obtained from the tables of Yeh and Lindau,[55] and the flux of the beamline. The depth profiling was performed on four positions and averaged. The average deviation from the mean is given as an error.

The wetting of a sample (compare Figure 4) was obtained by normalizing the O K-edge absorption spectra to their integrated intensities up to 533.5 eV. Because this pre-edge cannot belong to the contribution of liquid water, this normalization should scale the contributions of carbon−oxygen species also in the region above 534 eV, in which liquid water contributes. This procedure assumes that the carbonaceous species are similar in the compared samples. A reference of liquid water obtained by Schreck and Wernet[38] was fitted to the difference of two absorption spectra that should be compared by using a least-squares algorithm. The edge jump of the reference spectrum at 550 eV was used to determine the change in wetting.

■ ASSOCIATED CONTENT

Supporting Information

The Supporting Information is available free of charge at https://pubs.acs.org/doi/10.1021/acsami.0c08379.

Raman experiments on graphene quality, sample wetting, ionic conduction of polymer membranes, and in-situ gas detection (PDF)

https://dx.doi.org/10.1021/acsami.0c08379
ACS Appl. Mater. Interfaces 2020, 12, 37680−37692

AUTHOR INFORMATION

Corresponding Authors

Lorenz J. Falling − *Department of Inorganic Chemistry, Fritz-Haber-Institut der Max-Planck-Gesellschaft, 14195 Berlin, Germany;* orcid.org/0000-0002-2622-5166; Email: falling@fhi-berlin.mpg.de

Juan-Jesús Velasco-Vélez − *Department of Inorganic Chemistry, Fritz-Haber-Institut der Max-Planck-Gesellschaft, 14195 Berlin, Germany; Department of Heterogeneous Reactions, Max-Planck-Institut für Chemische Energiekonversion, 45470 Mülheim, Germany;* orcid.org/0000-0002-6595-0168; Email: velasco@fhi-berlin.mpg.de

Authors

Rik V. Mom − *Department of Inorganic Chemistry, Fritz-Haber-Institut der Max-Planck-Gesellschaft, 14195 Berlin, Germany;* orcid.org/0000-0002-5111-5591

Luis E. Sandoval Diaz − *Department of Inorganic Chemistry, Fritz-Haber-Institut der Max-Planck-Gesellschaft, 14195 Berlin, Germany*

Siamak Nakhaie − *Department of Inorganic Chemistry, Fritz-Haber-Institut der Max-Planck-Gesellschaft, 14195 Berlin, Germany*

Eugen Stotz − *Department of Inorganic Chemistry, Fritz-Haber-Institut der Max-Planck-Gesellschaft, 14195 Berlin, Germany*

Danail Ivanov − *Department of Inorganic Chemistry, Fritz-Haber-Institut der Max-Planck-Gesellschaft, 14195 Berlin, Germany*

Michael Hävecker − *Department of Inorganic Chemistry, Fritz-Haber-Institut der Max-Planck-Gesellschaft, 14195 Berlin, Germany; Department of Heterogeneous Reactions, Max-Planck-Institut für Chemische Energiekonversion, 45470 Mülheim, Germany*

Thomas Lunkenbein − *Department of Inorganic Chemistry, Fritz-Haber-Institut der Max-Planck-Gesellschaft, 14195 Berlin, Germany;* orcid.org/0000-0002-8957-4216

Axel Knop-Gericke − *Department of Inorganic Chemistry, Fritz-Haber-Institut der Max-Planck-Gesellschaft, 14195 Berlin, Germany; Department of Heterogeneous Reactions, Max-Planck-Institut für Chemische Energiekonversion, 45470 Mülheim, Germany*

Robert Schlögl − *Department of Inorganic Chemistry, Fritz-Haber-Institut der Max-Planck-Gesellschaft, 14195 Berlin, Germany; Department of Heterogeneous Reactions, Max-Planck-Institut für Chemische Energiekonversion, 45470 Mülheim, Germany*

Complete contact information is available at: https://pubs.acs.org/10.1021/acsami.0c08379

Notes

The authors declare no competing financial interest.

ACKNOWLEDGMENTS

The authors acknowledge the synchrotron radiation source BESSY II for the support during measurements and granting beamtime at the ISISS and UE56-2 PGM1 beamline, which is part of the Berlin Joint Laboratory for Electrochemical Interfaces (BElChem).

REFERENCES

(1) Ataka, K.; Yotsuyanagi, T.; Osawa, M. Potential-Dependent Reorientation of Water Molecules at an Electrode/Electrolyte Interface Studied by Surface-Enhanced Infrared Absorption Spectroscopy. *J. Phys. Chem.* **1996**, *100* (25), 10664−10672.

(2) Hunt, J. H.; Guyot-Sionnest, P.; Shen, Y. R. Observation of C-H Stretch Vibrations of Monolayers of Molecules Optical Sum-Frequency Generation. *Chem. Phys. Lett.* **1987**, *133* (3), 189−192.

(3) Axnanda, S.; Crumlin, E. J.; Mao, B.; Rani, S.; Chang, R.; Karlsson, P. G.; Edwards, M. O. M.; Lundqvist, M.; Moberg, R.; Ross, P.; Hussain, Z.; Liu, Z. Using "Tender" X-Ray Ambient Pressure X-Ray Photoelectron Spectroscopy as A Direct Probe of Solid-Liquid Interface. *Sci. Rep.* **2015**, *5*, 9788.

(4) Guo, H.; Strelcov, E.; Yulaev, A.; Wang, J.; Appathurai, N.; Urquhart, S.; Vinson, J.; Sahu, S.; Zwolak, M.; Kolmakov, A. Enabling Photoemission Electron Microscopy in Liquids via Graphene-Capped Microchannel Arrays. *Nano Lett.* **2017**, *17*, 1034−1041.

(5) Nemsak, S.; Strelcov, E.; Duchon, T.; Guo, H.; Hackl, J.; Yulaev, A.; Vlassiouk, I.; Mueller, D. N.; Schneider, C. M.; Kolmakov, A. Interfacial Electrochemistry in Liquids Probed with Photoemission Electron Microscopy. *J. Am. Chem. Soc.* **2017**, *139* (50), 18138−18141.

(6) Velasco-Velez, J. J.; Pfeifer, V.; Havecker, M.; Weatherup, R. S.; Arrigo, R.; Chuang, C.-H.; Stotz, E.; Weinberg, G.; Salmeron, M.; Schlogl, R.; Knop-Gericke, A. Photoelectron Spectroscopy at the Graphene-Liquid Interface Reveals the Electronic Structure of an Electrodeposited Cobalt/Graphene Electrocatalyst. *Angew. Chem., Int. Ed.* **2015**, *54* (48), 14554−14558.

(7) Knop-Gericke, A.; Pfeifer, V.; Velasco-Velez, J.-J.; Jones, T.; Arrigo, R.; Havecker, M.; Schlogl, R. In Situ X-Ray Photoelectron Spectroscopy of Electrochemically Active Solid-Gas and Solid-Liquid Interfaces. *J. Electron Spectrosc. Relat. Phenom.* **2017**, *221*, 10−17.

(8) Velasco-Vélez, J. J.; Jones, T. E.; Streibel, V.; Hävecker, M.; Chuang, C. H.; Frevel, L.; Plodinec, M.; Centeno, A.; Zurutuza, A.; Wang, R.; Arrigo, R.; Mom, R.; Hofmann, S.; Schlögl, R.; Knop-Gericke, A. Electrochemically Active Ir NPs on Graphene for OER in Acidic Aqueous Electrolyte Investigated by in Situ and Ex Situ Spectroscopies. *Surf. Sci.* **2019**, *681*, 1−8.

(9) Williamson, M. J.; Tromp, R. M.; Vereecken, P. M.; Hull, R.; Ross, F. M. Dynamic Microscopy of Nanoscale Cluster Growth at the Solid−Liquid Interface. *Nat. Mater.* **2003**, *2* (8), 532−536.

(10) Carbonio, E. A.; Velasco-Velez, J.-J.; Schlogl, R.; Knop-Gericke, A. Perspective—Outlook on Operando Photoelectron and Absorption Spectroscopy to Probe Catalysts at the Solid-Liquid Electrochemical Interface. *J. Electrochem. Soc.* **2020**, *167* (5), 054509.

(11) De Jonge, N.; Ross, F. M. Electron Microscopy of Specimens in Liquid. *Nat. Nanotechnol.* **2011**, *6* (11), 695−704.

(12) Ross, F. M. Opportunities and Challenges in Liquid Cell Electron Microscopy. *Science* **2015**, *350* (6267), aaa9886.

(13) Hodnik, N.; Dehm, G.; Mayrhofer, K. J. J. Importance and Challenges of Electrochemical in Situ Liquid Cell Electron Microscopy for Energy Conversion Research. *Acc. Chem. Res.* **2016**, *49* (9), 2015−2022.

(14) Arrigo, R.; Hävecker, M.; Schuster, M. E.; Ranjan, C.; Stotz, E.; Knop-Gericke, A.; Schlögl, R. In Situ Study of the Gas-Phase Electrolysis of Water on Platinum by NAP-XPS. *Angew. Chem., Int. Ed.* **2013**, *52* (44), 11660−11664.

(15) Sanchez Casalongue, H. G.; Ng, M. L.; Kaya, S.; Friebel, D.; Ogasawara, H.; Nilsson, A. In Situ Observation of Surface Species on Iridium Oxide Nanoparticles during the Oxygen Evolution Reaction. *Angew. Chem., Int. Ed.* **2014**, *53*, 7169−7172.

(16) Saveleva, V. A.; Papaefthimiou, V.; Daletou, M. K.; Doh, W. H.; Ulhaq-Bouillet, C.; Diebold, M.; Zafeiratos, S.; Savinova, E. R. Operando Near Ambient Pressure XPS (NAP-XPS) Study of the Pt Electrochemical Oxidation in H_2O and H_2O/O2 Ambients. *J. Phys. Chem. C* **2016**, *120* (29), 15930−15940.

(17) Pfeifer, V.; Jones, T. E.; Velasco Vélez, J. J.; Arrigo, R.; Piccinin, S.; Hävecker, M.; Knop-Gericke, A.; Schlögl, R. In Situ Observation of Reactive Oxygen Species Forming on Oxygen-Evolving Iridium Surfaces. *Chem. Sci.* **2017**, *8*, 2143−2149.

(18) Nappini, S.; Matruglio, A.; Naumenko, D.; Dal Zilio, S.; Bondino, F.; Lazzarino, M.; Magnano, E. Graphene Nanobubbles on

TiO_2 for In-Operando Electron Spectroscopy of Liquid-Phase Chemistry. *Nanoscale* **2017**, *9*, 4456−4466.
(19) Morozov, S. V.; Novoselov, K. S.; Katsnelson, M. I.; Schedin, F.; Elias, D. C.; Jaszczak, J. A.; Geim, A. K. Giant Intrinsic Carrier Mobilities in Graphene and Its Bilayer. *Phys. Rev. Lett.* **2008**, *100* (1), 11−14.
(20) Bolotin, K. I.; Sikes, K. J.; Hone, J.; Stormer, H. L.; Kim, P. Temperature-Dependent Transport in Suspended Graphene. *Phys. Rev. Lett.* **2008**, *101* (9), 1−4.
(21) Salvat, F.; Jabloski, A.; Powell, C. J. *NIST Standard Reference Database (SRD) 64*; National Institute of Standards and Technology: Gaithersburg, MD, 2002.
(22) Nair, R. R.; Blake, P.; Grigorenko, A. N.; Novoselov, K. S.; Booth, T. J.; Stauber, T.; Peres, N. M. R.; Geim, A. K. Fine Structure Constant Defines Visual Transparency of Graphene. *Science* **2008**, *320* (5881), 1308.
(23) Basov, D. N.; Fogler, M. M.; Lanzara, A.; Wang, F.; Zhang, Y. Colloquium: Graphene Spectroscopy. *Rev. Mod. Phys.* **2014**, *86* (3), 959−994.
(24) Mutus, J. Y.; Livadaru, L.; Robinson, J. T.; Urban, R.; Salomons, M. H.; Cloutier, M.; Wolkow, R. A. Low-Energy Electron Point Projection Microscopy of Suspended Graphene, the Ultimate "Microscope Slide. *New J. Phys.* **2011**, *13*, 063011.
(25) Longchamp, J.-N.; Latychevskaia, T.; Escher, C.; Fink, H.-W. Low-Energy Electron Transmission Imaging of Clusters on Free-Standing Graphene. *Appl. Phys. Lett.* **2012**, *101* (11), 113117.
(26) Miyauchi, H.; Ueda, Y.; Suzuki, Y.; Watanabe, K. Electron Transmission through Bilayer Graphene: A Time-Dependent First-Principles Study. *Phys. Rev. B: Condens. Matter Mater. Phys.* **2017**, *95* (12), 1−3.
(27) Frevel, L. J.; Mom, R.; Velasco-Velez, J.-J.; Plodinec, M.; Knop-Gericke, A.; Schlogl, R.; Jones, T. E. In Situ X-Ray Spectroscopy of the Electrochemical Development of Iridium Nanoparticles in Confined Electrolyte. *J. Phys. Chem. C* **2019**, *123* (14), 9146−9152.
(28) Mom, R.; Frevel, L.; Velasco-Velez, J.-J.; Plodinec, M.; Knop-Gericke, A.; Schlogl, R. The Oxidation of Platinum under Wet Conditions Observed by Electrochemical X-Ray Photoelectron Spectroscopy. *J. Am. Chem. Soc.* **2019**, *141* (16), 6537−6544.
(29) Velasco-Velez, J.-J.; Mom, R. V.; Sandoval-Diaz, L.-E.; Falling, L. J.; Chuang, C.-H.; Gao, D.; Jones, T. E.; Zhu, Q.; Arrigo, R.; Roldan Cuenya, B.; Knop-Gericke, A.; Lunkenbein, T.; Schlogl, R. Revealing the Active Phase of Copper during the Electroreduction of CO_2 in Aqueous Electrolyte by Correlating In Situ X-Ray Spectroscopy and In Situ Electron Microscopy. *ACS Energy Lett.* **2020**, *5* (6), 2106−2111.
(30) Martin, H. B.; Argoitia, A.; Landau, U.; Anderson, A. B.; Angus, J. C. Hydrogen and Oxygen Evolution on Boron-Doped Diamond Electrodes. *J. Electrochem. Soc.* **1996**, *143* (6), L133−136.
(31) Lehmani, A.; Durand-Vidal, S.; Turq, P. Surface Morphology of Nafion 117 Membrane by Tapping Mode Atomic Force Microscope. *J. Appl. Polym. Sci.* **1998**, *68* (3), 503−508.
(32) Ferrari, A. C.; Meyer, J. C.; Scardaci, V.; Casiraghi, C.; Lazzeri, M.; Mauri, F.; Piscanec, S.; Jiang, D.; Novoselov, K. S.; Roth, S.; Geim, A. K. Raman Spectrum of Graphene and Graphene Layers. *Phys. Rev. Lett.* **2006**, *97* (18), 1−4.
(33) Cancado, L. G.; Jorio, A.; Ferreira, E. H. M.; Stavale, F.; Achete, C. A.; Capaz, R. B.; Moutinho, M. V. O.; Lombardo, A.; Kulmala, T. S.; Ferrari, A. C. Quantifying Defects in Graphene via Raman Spectroscopy at Different Excitation Energies. *Nano Lett.* **2011**, *11* (8), 3190−3196.
(34) Strelcov, E.; Arble, C.; Guo, H.; Hoskins, B. D.; Yulaev, A.; Vlassiouk, I. V.; Zhitenev, N. B.; Tselev, A.; Kolmakov, A. Nanoscale Mapping of the Double Layer Potential at the Graphene-Electrolyte Interface. *Nano Lett.* **2020**, *20* (2), 1336−1344.
(35) Kraus, J.; Reichelt, R.; Gunther, S.; Gregoratti, L.; Amati, M.; Kiskinova, M.; Yulaev, A.; Vlassiouk, I.; Kolmakov, A. Photoelectron Spectroscopy of Wet and Gaseous Samples through Graphene Membranes. *Nanoscale* **2014**, *6* (23), 14394−14403.
(36) Velasco-Vélez, J. J.; Pfeifer, V.; Hävecker, M.; Wang, R.; Centeno, A.; Zurutuza, A.; Algara-Siller, G.; Stotz, E.; Skorupska, K.; Teschner, D.; Kube, P.; Braeuninger-Weimer, P.; Hofmann, S.; Schlögl, R.; Knop-Gericke, A. Atmospheric Ppressure X-Ray Photoelectron Spectroscopy Apparatus: Bridging the Pressure Gap. *Rev. Sci. Instrum.* **2016**, *87*, 053121.
(37) Ottosson, N.; Faubel, M.; Bradforth, S. E.; Jungwirth, P.; Winter, B. Photoelectron Spectroscopy of Liquid Water and Aqueous Solution: Electron Effective Attenuation Lengths and Emission-Angle Anisotropy. *J. Electron Spectrosc. Relat. Phenom.* **2010**, *177* (2−3), 60−70.
(38) Schreck, S.; Wernet, P. Isotope Effects in Liquid Water Probed by Transmission Mode X-Ray Absorption Spectroscopy at the Oxygen K-Edge. *J. Chem. Phys.* **2016**, *145*, 104502.
(39) Wernet, Ph; Nordlund, D.; Bergmann, U.; Cavalleri, M.; Odelius, N.; Ogasawara, H.; Näslund, L. Å.; Hirsch, T. K.; Ojamäe, L.; Glatzel, P.; Pettersson, L. G. M.; Nilsson, A. The Structure of the First Coordination Shell in Liquid Water. *Science* **2004**, *304* (5673), 995−999.
(40) Nilsson, A.; Nordlund, D.; Waluyo, I.; Huang, N.; Ogasawara, H.; Kaya, S.; Bergmann, U.; Näslund, L. Å.; Öström, H.; Wernet, Ph; Andersson, K. J.; Schiros, T.; Pettersson, L. G. M. X-Ray Absorption Spectroscopy and X-Ray Raman Scattering of Water and Ice; an Experimental View. *J. Electron Spectrosc. Relat. Phenom.* **2010**, *177*, 99−129.
(41) Yamazoe, K.; Higaki, Y.; Inutsuka, Y.; Miyawaki, J.; Cui, Y.-T.; Takahara, A.; Harada, Y. Enhancement of the Hydrogen-Bonding Network of Water Confined in a Polyelectrolyte Brush. *Langmuir* **2017**, *33* (16), 3954−3959.
(42) Cicero, G.; Grossman, J. C.; Schwegler, E.; Gygi, F.; Galli, G. Water Confined in Nanotubes and between Graphene Sheets: A First Principle Study. *J. Am. Chem. Soc.* **2008**, *130*, 1871−1878.
(43) Niskanen, J.; Sahle, C. J.; Juurinen, I.; Koskelo, J.; Lehtola, S.; Verbeni, R.; Müller, H.; Hakala, M.; Huotari, S. Protonation Dynamics and Hydrogen Bonding in Aqueous Sulfuric Acid. *J. Phys. Chem. B* **2015**, *119* (35), 11732−11739.
(44) Wren, A. G.; Phillips, R. W.; Tolentino, L. U. Surface Reactions of Chlorine Molecules and Atoms with Water and Sulfuric Acid at Low Temperatures. *J. Colloid Interface Sci.* **1979**, *70* (3), 544−557.
(45) Conway, B. E.; Mozota, J. Surface and Bulk Processes at Oxidized Iridium Electrodes-II. Conductivity-Switched Behaviour of Thick Oxide Films. *Electrochim. Acta* **1983**, *28*, 9−16.
(46) Kuo, D.-Y.; Kawasaki, J. K.; Nelson, J. N.; Kloppenburg, J.; Hautier, G.; Shen, K. M.; Schlom, D. G.; Suntivich, J. Influence of Surface Adsorption on the Oxygen Evolution Reaction on IrO_2 (110). *J. Am. Chem. Soc.* **2017**, *139* (9), 3473−3479.
(47) Jensen, E.; Købler, C.; Jensen, P. S.; Mølhave, K. In-Situ SEM Microchip Setup for Electrochemical Experiments with Water Based Solutions. *Ultramicroscopy* **2013**, *129*, 63−69.
(48) Møller-Nilsen, R. *In-Situ SEM Electrochemistry and Radiolysis*; Technical University of Denmark (DTU): 2016.
(49) Schneider, N. M.; Norton, M. M.; Mendel, B. J.; Grogan, J. M.; Ross, F. M.; Bau, H. H. Electron-Water Interactions and Implications for Liquid Cell Electron Microscopy. *J. Phys. Chem. C* **2014**, *118* (38), 22373−22382.
(50) Velasco-Velez, J.-J.; Jones, T.; Gao, D.; Carbonio, E.; Arrigo, R.; Hsu, C.-J.; Huang, Y.-C.; Dong, C.-L.; Chen, J.-M.; Lee, J.-F.; Strasser, P.; Roldan Cuenya, B.; Schlogl, R.; Knop-Gericke, A.; Chuang, C.-H. The Role of the Copper Oxidation State in the Electrocatalytic Reduction of CO_2 into Valuable Hydrocarbons. *ACS Sustainable Chem. Eng.* **2019**, *7* (1), 1485−1492.
(51) Mauritz, K. A.; Moore, R. B. State of Understanding of Nafion. *Chem. Rev.* **2004**, *104* (10), 4535−4585.
(52) Zawodzinski, T. A.; Neeman, M.; Sillerud, L. O.; Gottesfeld, S. Determination of Water Diffusion Coefficients in Perfluorosulfonate Ionomeric Membranes. *J. Phys. Chem.* **1991**, *95* (15), 6040−6044.
(53) L'Annunziata, M. F. Radiation Physics and Radionuclide Decay. In *Handbook of Radioactivity Analysis*; L'Annunziata, M. F., Ed.; Elsevier: Amsterdam, 2012; pp 1−162.

https://dx.doi.org/10.1021/acsami.0c08379
ACS Appl. Mater. Interfaces 2020, 12, 37680−37692

(54) Hävecker, M.; Cavalleri, M.; Herbert, R.; Follath, R.; Knop-Gericke, A.; Hess, C.; Hermann, K.; Schlögl, R. Methodology for the Structural Characterisation of V x O y Species Supported on Silica under Reaction Conditions by Means of in Situ O K-Edge X-Ray Absorption Spectroscopy. *Phys. Status Solidi B* **2009**, *246* (7), 1459−1469.
(55) Yeh, J. J.; Lindau, I. Atomic Subshell Photoionization Cross Sections and Asymmetry Parameters: 1 < Z < 103. *At. Data Nucl. Data Tables* **1985**, *32* (1), 1−155.

https://dx.doi.org/10.1021/acsami.0c08379
ACS Appl. Mater. Interfaces 2020, 12, 37680−37692